Article:
Xie 谢, Q 权, Liu 刘, J 佳, Erdélyi, R. et al. (2026) Inferring photospheric horizontal flows from multiple observations with SUVEL models. The Astrophysical Journal, 998 (2). 334. ISSN: 0004-637X

https://doi.org/10.3847/1538-4357/ae3ddf

The Astrophysical Journal, 998:334 (8pp), 2026 February 20 https://doi.org/10.3847/1538-4357/ae3ddf

Inferring Photospheric Horizontal Flows from Multiple Observations with SUVEL Models

Quan Xie (谢权)[1], Jiajia Liu (刘佳佳)[1,2], Robert Erdélyi[3,4,5], and Yuming Wang (汪毓明)[1,2]
[1] National Key Laboratory of Deep Space Exploration, School of Earth and Space Sciences, University of Science and Technology of China, Hefei 230026, People's Republic of China; jiajialiu@ustc.edu.cn
[2] CAS Center for Excellence in Comparative Planetology/CAS Key Laboratory of Geospace Environment/Mengcheng National Geophysical Observatory, University of Science and Technology of China, Hefei 230026, People's Republic of China
[3] Solar Physics & Space Plasma Research Center (SP2RC), School of Mathematical and Physical Sciences University of Sheffield, Hicks Building, Hounsfield Road, Sheffield S3 7RH, UK
[4] Department of Astronomy, Eötvös Loránd University, Pázmány Péter sétány 1/A, H-1112 Budapest, Hungary
[5] Hungarian Solar Physics Foundation, Petőfi tér 3, H-5700 Gyula, Hungary
Received 2025 November 30; revised 2026 January 11; accepted 2026 January 24; published 2026 February 19

Abstract

Photospheric horizontal velocity fields play essential roles in the formation and evolution of numerous solar activities. Various methods for estimating the horizontal velocity field have been proposed in the past. Aiming at the highest available (and future) spatial resolution (10 km pixel^{-1}) observations, a new method, the Shallow U-net models (SUVEL), based on realistic numerical simulation and machine learning techniques, was recently developed to track the photospheric horizontal velocity fields. Although SUVEL has been tested on numerical simulation data, its performance on solar observational data remained unclear. In this work, we apply SUVEL to the photospheric intensity observations from four ground-based solar telescopes (DKIST, GST, NVST, and SST) with the largest available apertures, and compare the results obtained from SUVEL with the Fourier local correlation tracking method (FLCT). Average correlation indices between granular regions and velocity fields inferred by SUVEL (FLCT) are 0.63, 0.81, 0.80, and 0.87 (0.00, 0.11, 0.16, and 0.10) for DKIST, GST, NVST, and SST observations. Higher correlation indices between the velocity fields tracked by SUVEL and granular patterns than FLCT reveal the superior performance of SUVEL, validating its reliability with respect to solar observational data.

Unified Astronomy Thesaurus concepts: Solar observatories (1513); Solar photosphere (1518); Solar granules (1875)

1. Introduction

The solar photosphere, the visible surface of the Sun, is a complex and highly dynamic system, and is filled with plasma flows. The most prominent features of the solar photosphere, including granulation, mesogranulation, and supergranulation, are all convective cells with different scales that originate in various depths in the convection zone beneath the photosphere. Horizontal flows play a key role in the formation and evolution of these cells. Moreover, abundant studies have revealed the associations between complex horizontal plasma motions and a range of solar phenomena, including small-scale photospheric vortices (e.g., Y. Wang et al. 1995; S. Wedemeyer-Böhm et al. 2012; J. Liu et al. 2019a, 2019b, 2019c, 2023; K. Tziotziou et al. 2023; Q. Xie et al. 2025b), sunspots (active regions; e.g., J. Evershed 1910; X. L. Yan & Z. Q. Qu 2007; Y. Bi et al. 2016; T. Gou et al. 2024), spicules, and jets (e.g., A. C. Sterling 2000; T. Matsumoto & K. Shibata 2010; J. Liu et al. 2016; H. Tian et al. 2021; S. Dey et al. 2022). Tracking the dynamic photospheric horizontal velocity fields contributes to investigations of the formation processes and mechanisms of these solar activities.

Up to now, various methods have been proposed to estimate the photospheric horizontal velocity fields. Feature tracking methods map the velocity fields by following the footprints of individual features in time-series images (see, e.g., L. H. Strous 1995). Then, several similar methods based on local correlation tracking (LCT; L. J. November & G. W. Simon 1988) are developed, including coherent structure tracking (M. Rieutord et al. 2007), Fourier local correlation tracking method (FLCT; B. T. Welsch et al. 2004; G. Fisher & B. Welsch 2008), differential affine velocity estimators (P. W. Schuck 2006), and nonlinear affine velocity estimators (J. Chae & T. Sakurai 2008). The above techniques accept the consecutive intensity images or line-of-sight (LOS) magnetograms as the input and have been applied to research from various aspects in solar physics (e.g., I. Giagkiozis et al. 2018; Y. Yuan et al. 2023).

Recently, machine (and deep) learning techniques have achieved rapid development and promoted significant progress in multiple fields, also conducing automatic tracking of solar horizontal velocity fields. A. Asensio Ramos et al. (2017) and B. Tremblay & R. Attie (2020) trained two neural networks using the numerical simulation data and published two models named *DeepVel* and *DeepVelU*, respectively. Due to the low spatial and temporal resolution of the training data, the performance of models in high-resolution data still requires improvement.

J. Liu et al. (2025) trained the shallow U-net models using high-resolution Bifrost (B. V. Gudiksen et al. 2011; M. Carlsson et al. 2016) numerical simulation data to track horizontal velocity fields from the highest available spatial resolution (∼10 km pixel^{-1}) observations provided by the Daniel K. Inouye Solar Telescope (DKIST; T. R. Rimmele et al. 2020). The models also aim to serve future telescopes,

Table 1
Summary of the Four Observations and Datasets Used in This Work

Obs No.	Telescope	Wavelength (nm)	Time Range	FOV Center	Region	Pixel Size	Cadence (s)	FOV Size (Mm)
1	DKIST /VBI	TiO (705)	2022-10-24 T19:47 ∼ 20:10	(−397″, 198″)	AR	0.″015 (11.1 km)	6.1	45 × 45
2	GST	TiO (705)	2025-08-16 T19:27 ∼ 22:17	(0″, 0″)	QS	0.″03 (22.2 km)	13	45 × 45
3	NVST	TiO (705)	2020-05-15 T01:17 ∼ 05:02	(0″, 0″)	QS	0.″052 (40 km)	30	102 × 86
4	SST /CRISP	Fe I (630.2)	2019-07-07 T08:23 ∼ 08:39	(0″, −300″)	QS	0.″059 (43.6 km)	4.2	41 × 42

Note. FOV refers to field of view. AR refers to active region. QS refers to quiet Sun. VBI refers to Visible Broadband Imager.

including the European Solar Telescope (4 m aperture, under construction; M. Collados et al. 2013), and the Chinese Giant Solar Telescope (8 m aperture, actively promoted; Z. Liu et al. 2013). The trained models have been integrated into a software package named SUVEL, available at the GitHub repository,[6] and the version used in this work is available on Zenodo at doi:10.5281/zenodo.18082382 (J. Liu 2025).

Although SUVEL has been tested and compared with FLCT on Bifrost and CO^{5}BOLD numerical simulation data (B. Freytag et al. 2012), it has not yet been comprehensively tested on solar observational data. In this work, we apply SUVEL to photospheric intensity images from multiple telescopes and compare the performance between SUVEL and FLCT, in order to validate the strength and advantages of SUVEL. In Section 2, we first briefly review SUVEL and then introduce the data used in this study. The results are presented in Section 3, followed by the whole summary of the paper and further discussions in Section 4.

2. Methods and Observations

U-net, proposed by O. Ronneberger et al. (2015), is widely used for segmentation tasks for biomedical images. Its name originates from the shape of its architecture, which resembles the letter "U." Some examples of its details and architecture can be found in Figure 2 in J. Liu et al. (2024) and J. Liu et al. (2025). Besides in biomedical sciences and other fields, the U-net neural network has also been employed for solar image segmentation and feature detection, e.g., the segmentation of coronal holes (E. A. Illarionov & A. G. Tlatov 2018), the detection of off-limb coronal jets (J. Liu et al. 2024) and sunspots (J. Chen et al. 2025), and the identification and tracking of filaments (Z. Zheng et al. 2024).

Based on a modified shallow U-net architecture, the photospheric intensity images obtained from the realistic 3D MHD simulation (M. Carlsson et al. 2016; J. Liu et al. 2025) were first used to train the intensity model with three consecutive intensity images as input. Considering the potential of LOS magnetograms to infer horizontal velocity fields (see, e.g., B. Tremblay & R. Attie 2020), the magnetic model, taking three consecutive frames of the vertical magnetic field strength, was also trained and built. Moreover, the third model, the hybrid model, takes three frames of simultaneous intensity and magnetic images, the output of the intensity model, and the output of the magnetic model as its input. Because the hybrid model learns from both photospheric intensity and vertical magnetic field strength, it was expected, and then proven, to perform better than the intensity and magnetic models. Therefore, SUVEL, with the architecture shown in Figure 1 in J. Liu et al. (2025), combining these three shallow U-net models, can not only take the single photospheric intensity images or LOS magnetograms as input, but also both of them.

It is worth noting that the performance of SUVEL on data with different pixel sizes and cadences was also tested. The results, shown in J. Liu et al. (2025), indicated that SUVEL generalizes well from the training conditions (10 km pixel^{-1} and 10 s cadence) to solar observations from most telescopes and satellites, covering pixel sizes of ∼10–160 km and cadences of ∼10–50 s.

To validate the performance of SUVEL on solar observational data, the data utilized in this study contain four datasets from four telescopes, respectively, including DKIST, the 1.6 m Goode Solar Telescope (GST; W. Cao et al. 2010), the New Vacuum Solar Telescope (NVST; Z. Liu et al. 2014), and the Swedish 1 m Solar Telescope (SST; G. B. Scharmer et al. 2003). Relevant information of the observations and properties of the corresponding data are summarized in Table 1.

All four observations are from the visible light band (TiO 705.7 nm wideband and Fe I 630.2 nm wideband), focusing on the photospheric surface layer. The cadences and pixel sizes are all suitable for SUVEL. The locations of the field of view (FOV) are plotted with red squares in the Helioseismic Magnetic Imager (HMI; P. H. Scherrer et al. 2012) magnetograms, shown in the top row in Figure 1, respectively.

The FOVs of SST and GST observations are tilted 70° clockwise and 23.°2 counterclockwise relative to the Sun's north pole, while the DKIST and NVST FOVs have no obvious rotations. Observations from GST, NVST, and SST target the quiet-Sun (QS) region, while the DKIST observations focus on an active region (AR). The bottom row presents four example intensity images from the datasets, captured by DKIST, GST, NVST, and SST, respectively. It is worth noting that we removed some empty areas near the boundary from the GST and NVST in this study. That is the reason why the sizes of the intensity images from GST and NVST (Figures 1(b2) and (c2)) are smaller than the FOV size shown in Table 1.

Following the procedure from J. Liu et al. (2025), the intensity images of all four datasets are first unified, respectively. For each frame, the image is divided by its mean intensity and then multiplied by the overall mean intensity of

[6] https://github.com/pydl/suvel

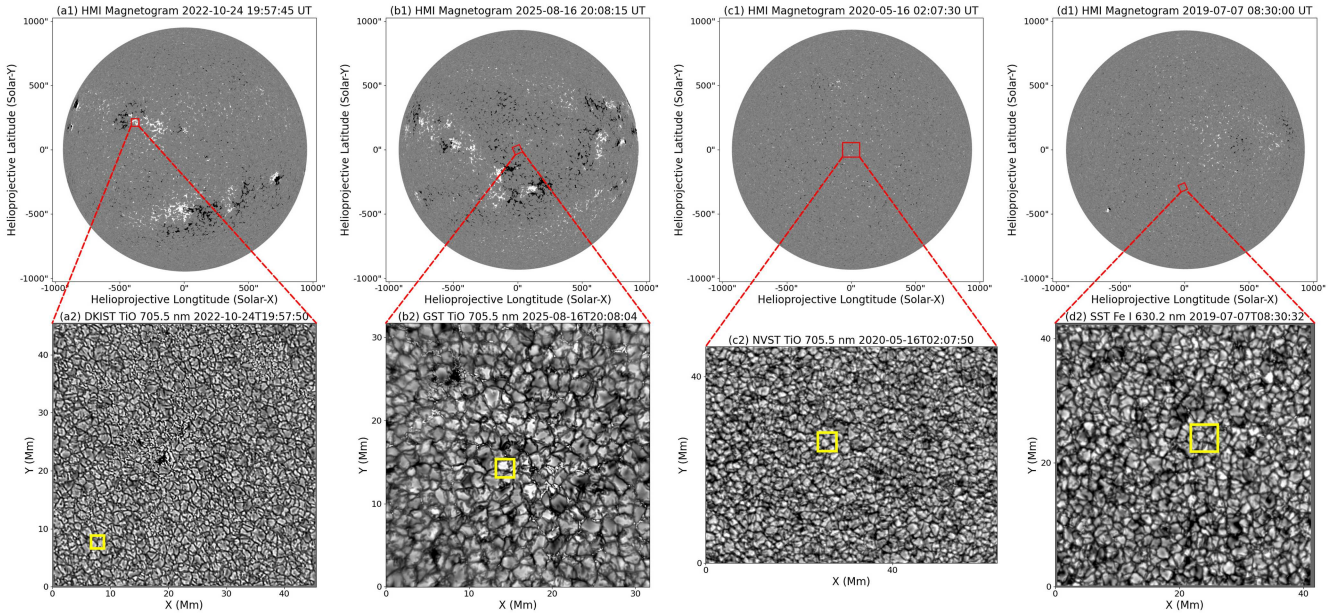

Figure 1. The four red squares drawn on the Solar Dynamics Observatory/HMI magnetograms in panels (a1)–(d1) depict the FOV locations of DKIST, GST, NVST, and SST observations, respectively. The bottom row shows four example intensity images of an instance in the four observations. The yellow squares outline the regions for further study.

the dataset. It ensures that all images of the four datasets have the same average intensity, respectively. Then, these unified intensity data are normalized to [0, 1] and input to the intensity model of SUVEL. The model output, velocity along the x-axis (v_{xi}) and velocity along the y-axis (v_{yi}), are rescaled to the real velocity (v_{xir} and v_{yir}) in units of km s^{-1}, based on Equation (6) in J. Liu et al. (2025) as follows:

$$v_{xir} = v_{xi} \cdot 23.4 - 11.7, \quad v_{yir} = v_{yi} \cdot 23.4 - 11.7. \tag{1}$$

The above unified and normalized intensity data are also utilized by FLCT to estimate the velocity fields. For the FLCT method utilized in this study, the local horizontal velocity field is obtained by maximizing the spatially localized cross-correlation between two consecutive intensity images. Following L. J. November & G. W. Simon (1988), let $J_t(\boldsymbol{x})$ and $J_{t+\tau}(\boldsymbol{x})$ denote the photospheric intensity images at times t and $t+\tau$, where the sampling time delay τ is also the cadence of the observation. The cross-correlation function at location $\boldsymbol{x}$ for a displacement vector $\boldsymbol{\delta}$ is defined as

$$C(\boldsymbol{\delta}, \boldsymbol{x}) = \int J_t\left(\boldsymbol{\xi} - \frac{\boldsymbol{\delta}}{2}\right) J_{t+\tau}\left(\boldsymbol{\xi} + \frac{\boldsymbol{\delta}}{2}\right) W_\sigma(\boldsymbol{x} - \boldsymbol{\xi})\, d^2\boldsymbol{\xi}. \tag{2}$$

Here, W_σ is an apodizing window that confines the correlation to a local neighborhood. Same as G. Fisher & B. Welsch (2008), we adopt a two-dimensional Gaussian window:

$$W_\sigma(\boldsymbol{s}) = \exp\left(-\frac{|\boldsymbol{s}|^2}{\sigma^2}\right), \tag{3}$$

where $\boldsymbol{s} = \boldsymbol{x} - \boldsymbol{\xi}$ is the relative displacement from the integration point $\boldsymbol{\xi}$ to the window center $\boldsymbol{x}$, and σ is the standard deviation of the Gaussian, serving as the fundamental spatial scale parameter in FLCT.

The parameters of FLCT are similar to the previous studies (see, e.g., J. Liu et al. 2019b, 2019c; Q. Xie et al. 2025b). However, it is worth noting that the Gaussian filter's σ is set specifically for each dataset to avoid some pixels moving outside the window. Assuming the maximum photospheric horizontal speed is 10 km s^{-1}, the maximum movement of a pixel is 10 km s^{-1} $\cdot$ dt/ds, with ds and dt representing the pixel size and cadence of the observation. Because a pixel can move in all directions, the value of sigma should be set twice the maximum movement. Therefore, the values of sigma are set to 15, 15, 15, and 10 for DKIST, GST, NVST, and SST datasets, respectively.

3. Results

3.1. Granules and Velocity Fields

The solar granulation pattern, first observed and described by W. Herschel (1801), was initially interpreted as arising from "hot clouds" floating above a cooler solar surface. Later, W. R. Dawes (1864) coined the term granules to describe the bright, irregularly shaped polygonal cells interspersed with narrow dark lanes. Subsequent Doppler shift measurements indicated localized upward motions within the granular regions (hereafter GRs) and downward motions within the intergranular lanes (hereafter IGLs). Thus, the dynamics of granulation can be understood as hot plasma rising in the GRs and cooler plasma descending in the IGLs. Consequently, velocity fields are expected to diverge in the GRs and converge within the IGLs.

We selected four small subregions from the four observational datasets, with their locations marked by yellow squares in Figures 1(a2)–(d2), to showcase the correlations between GRs and IGLs with the velocity fields derived from SUVEL and FLCT. Representative intensity images of the sampled regions are shown in the first row of Figure 2.

Several granules and the surrounding IGLs are clearly visible in these images (Figures 2(a1)–(d1)). In this study, pixels with intensities higher than $\mu + \sigma$ are identified as a GR, while those with intensities lower than $\mu - \sigma$ are classified as an IGL, where μ and σ denote the mean and standard deviation of the image intensity, respectively. The GR and IGL pixels are indicated by green and black dots in Figures 2(a2)–(d2).

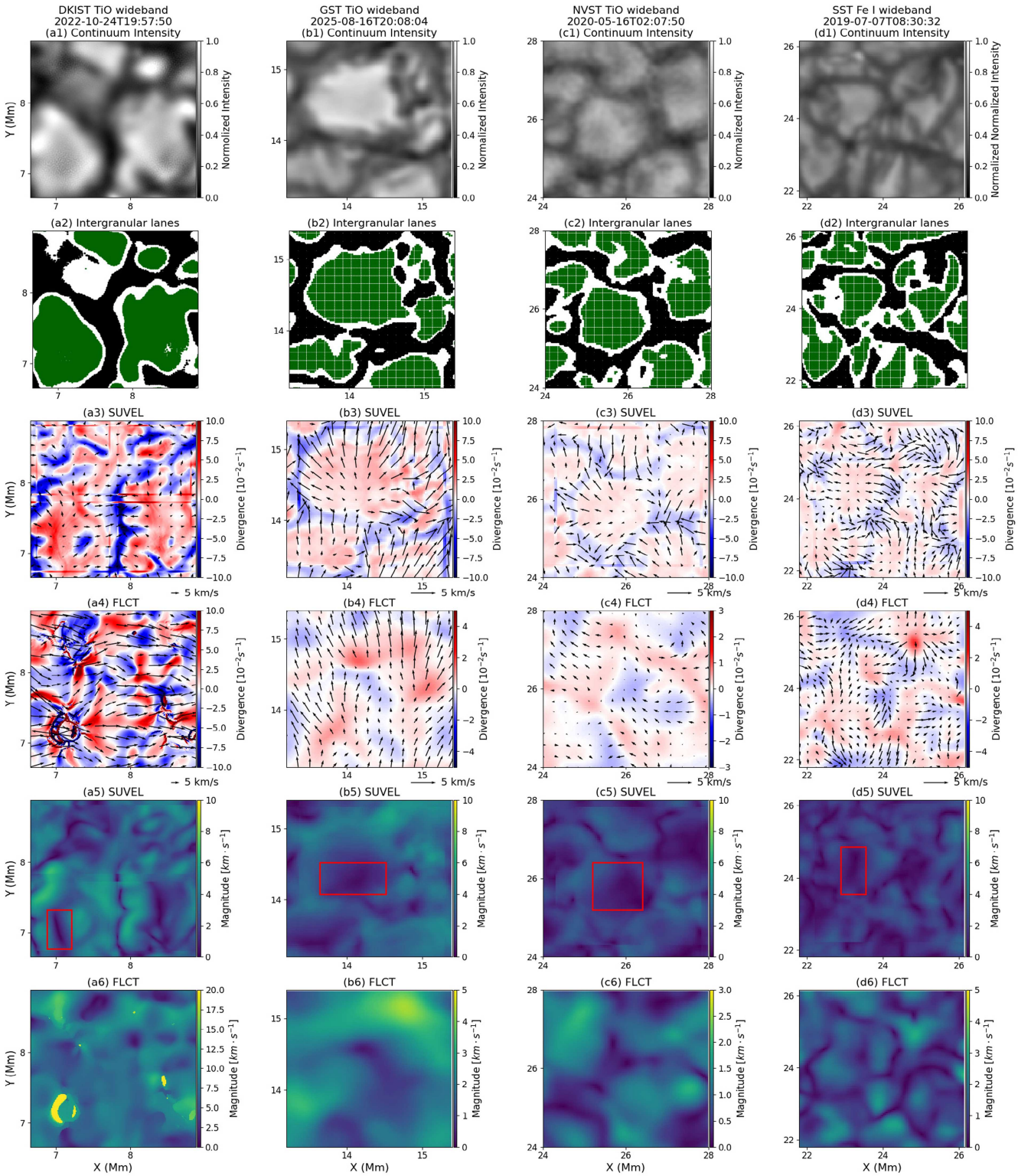

Figure 2. (a1)–(d1) Close-up views of the yellow boxes shown in Figure 1. (a2)–(d2) Green and black dots represent the granular regions and intergranular lanes. (a3)–(d3) The black arrows depict the velocity fields inferred by SUVEL, with the backgrounds showing the corresponding divergence maps. (a4)–(d4) Similar to (a3)–(d3), but for the velocity fields estimated by FLCT. (a5)–(d5) The magnitude maps of velocity fields inferred by SUVEL. (a6)–(d6) Similar to (a5)–(d5), but for the results of FLCT.

Black arrows in Figures 2(a3)–(d3) and (a4)–(d4) represent the velocity fields obtained from SUVEL and FLCT, respectively, overlaid on the corresponding divergence maps. For velocity along the x-axis (v_x) and velocity along the y-axis (v_y), the corresponding divergence map is calculated using the following formula:

$$\nabla \cdot \boldsymbol{v} = \left(\hat{\boldsymbol{i}}\frac{\partial}{\partial x} + \hat{\boldsymbol{j}}\frac{\partial}{\partial y}\right) \cdot (v_x\hat{\boldsymbol{i}} + v_y\hat{\boldsymbol{j}}) = \frac{\partial v_x}{\partial x} + \frac{\partial v_y}{\partial y}. \quad (4)$$

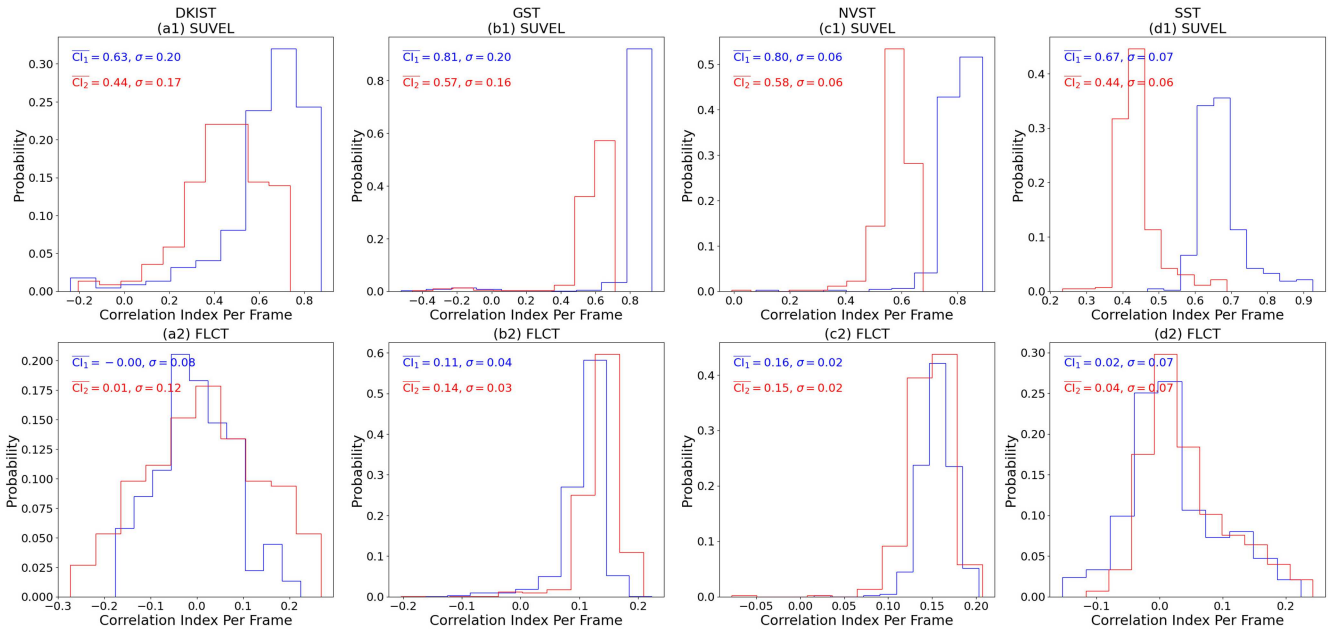

Figure 3. Per-frame average correlation indices between velocity fields and granulation patterns. CI_1 (blue) and CI_2 (red) depict the results of granular regions and intergranular lanes, respectively. (a1)–(d1) represent the results of the velocity fields inferred by SUVEL. (a2)–(d2) depict the results from FLCT.

Positive value means divergence, while a negative one represents convergence. Furthermore, Figures 2(a5)–(d5) and (a6)–(d6) show the velocity magnitude maps estimated by SUVEL and FLCT, respectively.

By comparing the divergence maps derived from SUVEL and FLCT with the corresponding intensity images, it is evident that the velocity fields tracked by SUVEL in all four observations are more consistent with the distributions of granules (GRs) and IGLs, exhibiting divergence in the GRs and convergence in the IGLs. In contrast, the performance of FLCT appears clearly unsatisfactory across all four observations. The correlation between the velocity fields obtained by FLCT and the spatial locations of the GRs and the IGLs is weak. To quantitatively assess this relationship, we propose a method, motivated by the approach of J. Liu et al. (2019c), to estimate the correlation between the velocity fields and the corresponding intensity structures.

First, based on the points of GRs and IGLs shown in Figures 2(a2)–(d2), we set all GR points to one and all other points to zero, generating the GR binary intensity map I_1. Similarly, for the IGL binary intensity map I_2, all IGL points are set as -1, with other points set as zero. The total number of all GR and IGL points is N_G and N_{IG}.

Then, divergence maps D are calculated from the horizontal maps estimated by SUVEL and FLCT, using Equation (4). Furthermore, the sign map D_s of the divergence map D is obtained, meaning all positive values in D are set as 1, and all negative values are set as -1.

Lastly, we combine $I_1(I_2)$ and D_s through a Hadamard product, and obtain the correlation map C_1 (C_2) of the GRs (and the IGLs), respectively. Correlation indices CI_1 (and CI_2) between the GRs (and the IGLs) and velocity fields are calculated correspondingly with the following equation:

$$CI_1 = \left(\sum C_1\right)/N_G, \quad CI_2 = \left(\sum C_2\right)/N_{IG}. \tag{5}$$

The above procedures indicate that correlation indices (CIs) are concentrated on $[-1, 1]$, with higher values implying higher relations. Correlation indices (CI_1 and CI_2) of all frames in the four observations are calculated, using the velocity fields estimated by SUVEL and FLCT, respectively.

Shown in Figure 3, statistical results indicate that the average CIs between the GRs and velocity fields inferred by SUVEL are 0.63, 0.81, 0.80, and 0.87 for DKIST, GST, NVST, and SST observations, all higher than the results (0.00, 0.11, 0.16, and 0.10) from FLCT. A similar priority also holds for the IGLs, suggesting that SUVEL provides better and more reliable photospheric horizontal velocity field estimation than FLCT.

Comparing the distributions of CI_1 and CI_2 from SUVEL, shown in Figures 3(a1)–(d1), it is worth noting that SUVEL tracks velocity fields less effectively in the IGLs than in granules. We suggest that one of the reasons is the intrinsic limitations of SUVEL. J. Liu et al. (2025) noted that SUVEL still exhibits certain shortcomings and requires further improvement, particularly when applied to regions rich in small-scale structures, due to the nature of the U-NET neural network architecture. IGLs and their surrounding regions are where small-scale structures are densely concentrated (e.g., Å. Nordlund et al. 2009), which influences the velocity field reconstruction of SUVEL. A key point of future work is to focus on the improvement of SUVEL on such small-scale structures.

Next, let us also apply the method to the Bifrost numerical simulation data (details see J. Liu et al. 2025), which was used for the training and testing of SUVEL models. Instead of applying estimated velocity fields, we adopt simulated intensity images and their corresponding velocity fields to calculate the average CIs for the GRs and the IGLs. CIs of the GRs and the IGLs are 0.70 ± 0.05 and 0.51 ± 0.03, respectively. These results are close to the results of SUVEL obtained from the above various observations, again, supporting the reliability of SUVEL.

Moreover, focusing on the magnitude distribution of the velocity fields derived by SUVEL, one can notice that there is

usually a small region within a granule with low horizontal speeds. The red squares in panels (a5)–(d5) in Figure 2 mark four example positions. Naturally, a cloud of cool plasma arises onto the surface from the layer beneath, experiencing low horizontal speeds corresponding to the red squares in Figures 2(a5)–(d5). The plasma then spreads out, contributing to the divergent flows inside GRs. The plasma moves faster and faster, reaching its peak speed in the IGLs. Bunches of rapid plasma flows from neighboring granules gather together and begin to sink due to their relatively low temperature. This also naturally causes the relatively low horizontal velocities at the IGLs, which can be seen when comparing panels (a3)–(d3) and panels (a5)–(d5) in Figure 2.

Let us now turn our attention to the velocity fields estimated by FLCT, shown in panels (a4)–(d4) and (a6)–(d6) in Figure 2. Although FLCT can also capture some details, most structures, especially the boundaries between GRs and IGLs, disappear. M. Verma et al. (2013) used CO^{5}BOLD numerical simulation data to evaluate LCT, suggesting that LCT underestimates the speed by a factor of approximately 3. Comparisons between velocity fields, derived by SUVEL and FLCT from GST, NVST, and SST observations, also indicate a similar underestimation of velocity fields estimated by FLCT as SUVEL, shown in Figures 2(b5)–(d5) and (b6)–(d6). This finding further proves the accuracy of SUVEL and supports the previous findings using observational evidence. However, for DKIST observations, it is seen that FLCT infers larger speeds than SUVEL, shown in Figures 2(a5) and (a6). These significantly larger speeds (exceeding 20 km s^{-1} in the yellow regions in Figure 2(a6)) should not be real, given that the sound speed and Alfvén speed in the photosphere are generally less than 10 km s^{-1}. These unrealistic large speeds may be attributed to the high spatial resolution (11.1 km pixel^{-1}), which influences the performance of FLCT.

In summary, based on the above results and analysis, we conclude that SUVEL models can credibly reconstruct the photospheric horizontal velocity fields from the observations of different telescopes, proving the usability on observational data.

3.2. Influence on Vortex Detections

Ubiquitous small-scale velocity/plasma vortices are found in the photosphere, which are primarily located in the IGLs (see, e.g., I. Giagkiozis et al. 2018; J. Liu et al. 2019b; K. Tziotziou et al. 2023). Recently, Q. Xie et al. (2025b) found that many small-scale vortices tend to be located at larger scales in intermesogranular lanes, offering a new perspective on the depth at which such small-scale vortices form beneath the solar photosphere. Photospheric vortices were generally believed to be associated with coronal heating (e.g., J. B. Zirker 1993). J. Liu et al. (2019c) showed that vortices transport energy from the photosphere to the upper chromosphere. Note that these small-scale vortices are not easy to identify with the human eye. Various methods have been developed to reduce the biases and limitations inherent in manual detection. For example, based on the Γ-functions method proposed by L. Graftieaux et al. (2001), J. Liu et al. (2019b) developed and made the automated swirl detection algorithm (ASDA) openly available to identify vortices from estimated photospheric horizontal velocity fields. The algorithm (and the Γ-functions method) was recently improved by Q. Xie et al. (2025a), named as the Optimized ASDA and available at the GitHub repository,[7] resulting in improved detection rates and accuracies of such small-scale vortices. The version used in this work is available in Zenodo at doi:10.5281/zenodo.18074489 (Q. Xie et al. 2026).

Previous studies are mostly dependent on the velocity fields derived from FLCT (e.g., I. Giagkiozis et al. 2018; J. Liu et al. 2019b, 2019c; Q. Xie et al. 2025b). However, as mentioned before, the performances of FLCT do not seem as precise as expected. K. Tziotziou et al. (2023) also pointed out that very small photospheric vortices might be ignored by LCT methods. Therefore, to explore how different velocity tracking methods (SUVEL and FLCT) influence the vortex detection, we employ the Optimized ASDA with velocity fields tracked by SUVEL and FLCT from the DKIST, GST, NVST, and SST observations, introduced in Section 2.

Figure 4 depicts the average number of vortices detected per frame using SUVEL and FLCT with the Optimized ASDA from DKIST, GST, NVST, and SST observations, respectively. N_p and N_n denote the number of positive (counterclockwise rotation) and negative (clockwise rotation) vortices, distinguished by blue and red, respectively. The average number of all vortices per frame is represented by N in black. We note that vortices, detected from DKIST intensity images, whose radii are less than 5 pixels, are omitted, because the diffraction limit of the TiO 705 nm band for DKIST is estimated approximately $0\farcs038$ (2.5 pixels). The number densities of vortices are found to be 0.47, 0.32, 0.17, and 0.29 Mm^{-2} using SUVEL on the observations from DKIST, GST, NVST, and SST, respectively. On the other hand, using FLCT, the number densities are 0.32, 0.09, 0.08, and 0.17 Mm^{-2}. Considering the different spatial resolutions of the four telescopes, it is found that the number densities are nearly positively related to the pixel sizes of observations. N. Yadav et al. (2020) pointed out that larger vortices detected from low-spatial-resolution observations may consist of several smaller vortices detected from high-resolution data, explaining why more vortices are detected from high-resolution data. This is consistent with the above findings that the most significant number densities of vortices are found with DKIST observations, no matter which horizontal velocity field tracking method has been used.

Comparing the vortex numbers estimated by SUVEL and FLCT, it is evident that the vortex numbers from FLCT are all lower than those from SUVEL for all four observations. Therefore, FLCT might lead to an underestimation of vortex number (density). Moreover, the densities from the four datasets are approximately 0.3 Mm^{-2}, significantly greater than almost all previous results, e.g., 2.2×10^{-2} Mm^{-1} (J. A. Bonet et al. 2010), 6.1×10^{-2} Mm^{-1} (J. Liu et al. 2019c), and 2.11×10^{-2} Mm^{-1} (Q. Xie et al. 2025b). In addition to SUVEL, another factor contributing to the more detection is that the Optimized ASDA could miss fewer vortices than the original ASDA, as suggested in Q. Xie et al. (2025a).

We also investigated the distributions of vortex radius, rotation speed, and expansion/contraction speed derived from the four observations using SUVEL. Vortices with smaller radii are detected in higher-resolution observations, suggesting that even smaller vortices could exist in the solar atmosphere. Rotation speeds are all found around 2 km s^{-1}, which are consistent with some previous studies (e.g., S. Wedemeyer-Böhm &

[7] https://github.com/dreamstar0831/Optimized_ASDA

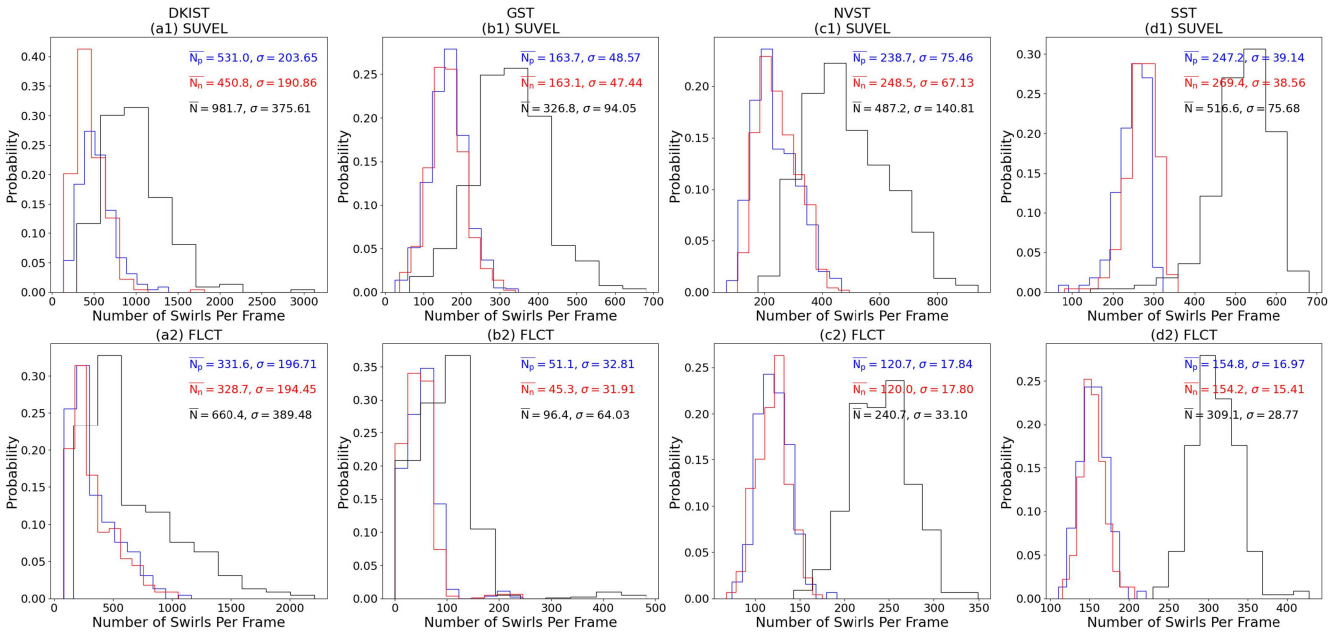

Figure 4. Per-frame average number of detected vortices. Subscripts p and n (blue and red) denote positive and negative vortices, respectively. Black curves and texts are the results of all swirls. σ represents the standard deviation. (a1)–(d1) Number of vortices detected by the Optimized ASDA and SUVEL from the DKIST, GST, NVST, and SST observations. (a2)–(d2) Similar to the top panels, but for the results of FLCT.

L. Rouppe van der Voort 2009), especially with our previous results from numerical simulations (J. Liu et al. 2019a), but higher than those found with FLCT (J. Liu et al. 2019b), shedding light on the real rotation speed of photospheric vortices (J. R. Canivete Cuissa & O. Steiner 2024). Expansion (contraction) speeds are approximately 0.5 (-0.6) km s^{-1}, again, larger than $\sim$0.2 (-0.2) km s^{-1} in previous studies (J. Liu et al. 2019b, 2019c; Q. Xie et al. 2025b). Therefore, combining SUVEL with the Optimized ASDA enables more vortices to be detected with higher accuracy in their positions, radii, expansion speeds, and other properties, contributing to further detailed studies of photospheric vortices.

4. Conclusion and Discussions

In this study, we applied the newly developed horizontal velocity field estimation model SUVEL to solar observations from multiple telescopes (DKIST, GST, NVST, and SST) to validate the strength and advantages of SUVEL. The main results of this work are summarized as follows.

1. By sampling four small regions of an instance from the four observations, we intuitively discover that velocity fields derived by SUVEL match the corresponding granular pattern better than the ones estimated by FLCT. We then propose a method to calculate the correlation indices between the velocity fields and intensity structures. Higher correlation indices of all four observations further prove the priority of SUVEL.
2. We combined the Optimized ASDA with SUVEL and FLCT to detect photospheric vortices. More vortices are identified using SUVEL than using FLCT, indicating that FLCT underestimates the vortex number in previous studies. The open-source software SUVEL can provide better and more reliable results for public use. It is worth noting that the number of true vortices detected by SUVEL and FLCT is still unclear. Future work focusing on the one-to-one comparisons between vortices detected from SUVEL (FLCT) and the real vortices identified from the simulated velocity fields will further reveal the accuracy of SUVEL and FLCT on photospheric horizontal velocity field reconstruction.

Larger vortex densities also indicate the great potential of combining SUVEL with the Optimized ASDA for photospheric vortex detection. Although the influence of SUVEL and the Optimized ASDA on vortex detection has been discussed in Section 3, the influence on the estimation of vortex lifetime is still under exploration. J. Liu et al. (2019b) proposed a method to estimate the lifetime and found that most vortices have lifetimes less than twice the cadences. We speculate that the results may be affected by the inaccurate velocity fields estimated by FLCT. In future work, we will also focus on the study of vortex lifetime using SUVEL and the Optimized ASDA to provide more precise lifetime distributions of photospheric vortices.

Acknowledgments

J.L. and Q.X. acknowledge the support from the Strategic Priority Research Program of the Chinese Academy of Science (grant No. XDB0560000), the National Natural Science Foundation (NSFC 42188101 and 12373056), and China's Space Origins Exploration Program. R.E. acknowledges the NKFIH (OTKA, grant No. K142987), Hungary, for enabling this research. R.E. is also grateful to the Science and Technology Facilities Council (STFC, grant No. ST/M000826/1) UK, PIFI (China, grant No. 2024PVA0043), and the NKFIH Excellence Grant TKP2021-NKTA-64 (Hungary). We acknowledge the use of Swedish 1 m Solar Telescope (SST) data. SST is operated on the island of La Palma (Spain) by the Institute for Solar Physics of Stockholm University in the Spanish Observatorio del Roque de los Muchachos of the Instituto de Astrofísica de Canarias. The research reported herein is based in part on data collected with the Daniel K. Inouye Solar Telescope (DKIST), a facility of

the U.S. National Science Foundation. The National Solar Observatory operates DKIST under a cooperative agreement with the Association of Universities for Research in Astronomy, Inc. DKIST is located on land of spiritual and cultural significance to Native Hawaiian people. The use of this important site to further scientific knowledge is done with appreciation and respect. This research is also supported by the International Space Science Institute (ISSI) in Beijing.

ORCID iDs

Quan Xie (谢权) https://orcid.org/0009-0008-8972-2726
Jiajia Liu (刘佳佳) https://orcid.org/0000-0003-2569-1840
Robert Erdélyi https://orcid.org/0000-0003-3439-4127
Yuming Wang (汪毓明) https://orcid.org/0000-0002-8887-3919

References

Asensio Ramos, A., Requerey, I. S., & Vitas, N. 2017, A&A, 604, A11
Bi, Y., Jiang, Y., Yang, J., et al. 2016, NatCo, 7, 13798
Bonet, J. A., Márquez, I., Sánchez Almeida, J., et al. 2010, ApJL, 723, L139
Canivete Cuissa, J. R., & Steiner, O. 2024, A&A, 682, A181
Cao, W., Gorceix, N., Coulter, R., et al. 2010, AN, 331, 636
Carlsson, M., Hansteen, V. H., Gudiksen, B. V., Leenaarts, J., & De Pontieu, B. 2016, A&A, 585, A4
Chae, J., & Sakurai, T. 2008, ApJ, 689, 593
Chen, J., Gyenge, N. G., Jiang, Y., et al. 2025, ApJ, 980, 261
Collados, M., Bettonvil, F., Cavaller, L., et al. 2013, MmSAI, 84, 379
Dawes, W. R. 1864, MNRAS, 24, 161
Dey, S., Chatterjee, P., O. V. S. N., M., et al. 2022, NatPh, 18, 595
Evershed, J. 1910, MNRAS, 70, 217
Fisher, G., & Welsch, B. 2008, ASPC, 383, 373
Freytag, B., Steffen, M., Ludwig, H.-G., et al. 2012, JCoPh, 231, 919
Giagkiozis, I., Fedun, V., Scullion, E., Jess, D. B., & Verth, G. 2018, ApJ, 869, 169
Gou, T., Liu, R., Su, Y., et al. 2024, SoPh, 299, 99
Graftieaux, L., Michard, M., & Grosjean, N. 2001, MeScT, 12, 1422
Gudiksen, B. V., Carlsson, M., Hansteen, V. H., et al. 2011, A&A, 531, A154
Herschel, W. 1801, RSPT, 91, 265
Illarionov, E. A., & Tlatov, A. G. 2018, MNRAS, 481, 5014
Liu, J. 2025, SUVEL—Tracking the Photospheric Horizontal Velocity Field with Shallow UNet Models v1.0, Zenodo, doi:10.5281/zenodo.18082382
Liu, J., Carlsson, M., Nelson, C. J., & Erdélyi, R. 2019a, A&A, 632, A97
Liu, J., Jess, D., Erdélyi, R., & Mathioudakis, M. 2023, A&A, 674, A142
Liu, J., Ji, C., Wang, Y., et al. 2024, ApJ, 972, 187
Liu, J., Nelson, C. J., & Erdélyi, R. 2019b, ApJ, 872, 22
Liu, J., Nelson, C. J., Snow, B., Wang, Y., & Erdélyi, R. 2019c, NatCo, 10, 3504
Liu, J., Wang, Y., Erdélyi, R., et al. 2016, ApJ, 833, 150
Liu, J., Xie, Q., Zhong, C., et al. 2025, A&A, 698, A263
Liu, Z., Deng, Y., & Ji, H. 2013, IAUS, 300, 349
Liu, Z., Xu, J., Gu, B.-Z., et al. 2014, RAA, 14, 705
Matsumoto, T., & Shibata, K. 2010, ApJ, 710, 1857
Nordlund, Å., Stein, R. F., & Asplund, M. 2009, LRSP, 6, 2
November, L. J., & Simon, G. W. 1988, ApJ, 333, 427
Rieutord, M., Roudier, T., Roques, S., & Ducottet, C. 2007, A&A, 471, 687
Rimmele, T. R., Warner, M., Keil, S. L., et al. 2020, SoPh, 295, 172
Ronneberger, O., Fischer, P., & Brox, T. 2015, in Medical Image Computing and Computer-Assisted Intervention—MICCAI 2015, ed. N. Navab et al. (Springer), 234
Scharmer, G. B., Bjelksjo, K., Korhonen, T. K., Lindberg, B., & Petterson, B. 2003, SPIE, 4853, 341
Scherrer, P. H., Schou, J., Bush, R., et al. 2012, SoPh, 275, 207
Schuck, P. W. 2006, ApJ, 646, 1358
Sterling, A. C. 2000, SoPh, 196, 79
Strous, L. H. 1995, in Helioseismology, ed. J. T. Hoeksema et al. (ESA), 219
Tian, H., Harra, L., Baker, D., Brooks, D. H., & Xia, L. 2021, SoPh, 296, 47
Tremblay, B., & Attie, R. 2020, FrASS, 7, 25
Tziotziou, K., Scullion, E., Shelyag, S., et al. 2023, SSRv, 219, 1
Verma, M., Steffen, M., & Denker, C. 2013, A&A, 555, A136
Wang, Y., Noyes, R. W., Tarbell, T. D., et al. 1995, Study of Magnetic Notions in the Solar Photosphere and Their Implications for Heating the Solar Atmosphere NAS 1.26:200084, Smithsonian Astrophysical Observatory, https://ntrs.nasa.gov/citations/19960012480
Wedemeyer-Böhm, S., & Rouppe van der Voort, L. 2009, A&A, 507, L9
Wedemeyer-Böhm, S., Scullion, E., Steiner, O., et al. 2012, Natur, 486, 505
Welsch, B. T., Fisher, G. H., Abbett, W. P., & Regnier, S. 2004, ApJ, 610, 1148
Xie, Q., Liu, J., Erdélyi, R., & Wang, Y. 2025a, A&A, 700, A6
Xie, Q., Liu, J., Erdélyi, R., & Wang, Y. 2026, Optimized Automated Swirl Detection Algorithms v1.0, Zenodo, doi:10.5281/zenodo.18074489
Xie, Q., Liu, J., Nelson, C. J., Erdélyi, R., & Wang, Y. 2025b, ApJ, 979, 27
Yadav, N., Cameron, R. H., & Solanki, S. K. 2020, ApJL, 894, L17
Yan, X. L., & Qu, Z. Q. 2007, A&A, 468, 1083
Yuan, Y., de Souza e Almeida Silva, S., Fedun, V., Kitiashvili, I. N., & Verth, G. 2023, ApJS, 267, 35
Zheng, Z., Hao, Q., Qiu, Y., et al. 2024, ApJ, 965, 150
Zirker, J. B. 1993, SoPh, 147, 47